

# Magnetoresistance and electronic structure of asymmetric GaAs/Al<sub>0.3</sub>Ga<sub>0.7</sub>As double quantum wells in the in-plane/tilted magnetic field

O. N. Makarovskii<sup>1,2</sup>, L. Smrčka<sup>1</sup>, P. Vašek<sup>1</sup>, T. Jungwirth<sup>1,3</sup>, M. Cukr<sup>1</sup>, L. Jansen<sup>4</sup>

<sup>1</sup>*Institute of Physics ASCR, Cukrovarnická 10, 162 53 Praha 6, Czech Republic*

<sup>2</sup>*Institute of Radiophysics and Electronics, NAS Ukr. Kharkov, Ukraine*

<sup>3</sup>*Department of Physics, Indiana University, Bloomington, Indiana 47405*

<sup>4</sup>*Grenoble High Magnetic Field Laboratory, BP 166, 38042 Grenoble Cedex 09, France*

(February 1, 2008)

Bilayer two-dimensional electron systems formed by a thin barrier in the GaAs buffer of a standard heterostructure were investigated by magnetotransport measurements. In magnetic fields oriented parallel to the electron layers, the magnetoresistance exhibits an oscillation associated with the de-population of the higher occupied subband and the field-induced transition into a decoupled bilayer. Shubnikov-de Haas oscillations in slightly tilted magnetic fields allow to reconstruct the evolution of the electron concentration in the individual subbands as a function of the in-plane magnetic field. The characteristics of the system derived experimentally are in *quantitative* agreement with numerical self-consistent-field calculations of the electronic structure.

PACS numbers: 73.20.Dx, 73.40.-c, 73.50.-h

## I. INTRODUCTION

In an idealized, infinitely narrow two-dimensional (2D) system the in-plane component of the magnetic field couples only to the electronic spin degree of freedom. In real samples, however, the finite size of a 2D system in the growth ( $\hat{z}$ ) direction often leads to strong orbital effects of the in-plane field. For example, 2D-2D tunneling studies<sup>1</sup> of a system consisting of two nearby narrow quantum wells, which is the simplest structure with non-trivial growth direction degree of freedom, have revealed dramatic effects of the in-plane field on the Fermi surface topology. In this weakly-coupled double quantum well sample the in-plane field,  $B_{\parallel}$ , in effect displaces the origin of the two layer Fermi circles by  $|e|B_{\parallel}d/\hbar$  and allows a sweep of one past the other at a critical field  $B_c = 2\hbar k_F/|e|d$ , where  $d$  is the layer separation and  $k_F$  is the individual layer Fermi wavevector.

The crossing of Fermi surfaces is replaced with more complicated patterns in samples with strongly coupled quantum wells in which the tunneling rate dominates the electronic scattering rate within a well. In a simple tight-binding model<sup>2</sup> a partial energy gap, equal to the bonding-antibonding gap at zero field, opens at the wavevector corresponding to the crossing point of the displaced dispersion curves for the uncoupled layers. While the upper subband above the energy gap maintains a nearly parabolic shape, a saddle point develops in the lower energy subband. With increasing  $B_{\parallel}$  the bottom of the upper subband moves above the Fermi energy at a critical field  $B_{c,1}$ , resulting in a sudden drop in the density of states. At the second critical field,  $B_{c,2}$ , the saddle point of the lower subband approaches the Fermi energy and the density of states diverges. The magnetoresistance oscillation observed on coupled double<sup>3,4</sup> and triple<sup>5</sup> quantum wells represents a striking manifes-

tation of the two distinct van Hove singularities in the  $B_{\parallel}$ -dependent density of states. For these samples the tight-binding model has provided an accurate quantitative estimate for the critical in-plane fields. Bilayer systems realized in wide single quantum wells also display<sup>6</sup> the magnetoresistance oscillation, however, the orbital effects of the in-plane magnetic field are more complex here and cannot be captured by the simple tight-binding approximation. Instead, the numerical self-consistent-field technique has proven successful<sup>6</sup> for wide quantum wells.

The importance of orbital effects of the in-plane magnetic field has recently been emphasized<sup>7</sup> also in the context of metal-insulator transition studies in Si-MOSFET<sup>8</sup> and GaAs/Al<sub>0.3</sub>Ga<sub>0.7</sub>As single heterojunctions.<sup>9,10</sup> The observed dramatic response to  $B_{\parallel}$  in both metallic and insulating phases has been attributed<sup>7,10</sup> to the spin coupling to in-plane field as well as to the distortion<sup>11,12</sup> of carrier Fermi surfaces. A detailed quantitative understanding of these phenomena requires to incorporate the orbital effects of  $B_{\parallel}$  using non-perturbative approaches.

In this paper we present a study of magnetotransport properties of GaAs/Al<sub>0.3</sub>Ga<sub>0.7</sub>As heterojunctions with an additional thin Al<sub>0.3</sub>Ga<sub>0.7</sub>As barrier introduced into the GaAs buffer.<sup>13</sup> The structures were specially designed to combine properties of single-junction and bilayer systems. A comparison between theory and experiment in our samples constitutes an excellent test for the reliability of the numerical self-consistent-field technique applied to systems with complex growth direction geometries. In Section II we present measured resistance oscillation with in-plane field and Shubnikov-de Haas (SdH) oscillations recorded at magnetic fields slightly tilted from the 2D layer plane. Theoretical calculations of the  $B_{\parallel}$ -dependent electronic structure are used, in Section III, for quantitative interpretation of the experimental data. Our conclusions are summarized in Section IV.

## II. EXPERIMENTAL RESULTS

We studied modulation-doped GaAs/Al<sub>0.3</sub>Ga<sub>0.7</sub>As heterojunctions grown by molecular-beam epitaxy on (100) oriented semi-insulating GaAs substrates and patterned in the standard Hall-bar samples. A thin barrier formed by eight monolayers of Al<sub>0.3</sub>Ga<sub>0.7</sub>As was grown inside the GaAs buffer producing two coupled quantum wells, one of a distorted rectangular shape and the other one with a nearly triangular geometry, as shown in insets of Fig. 1. We chose the thickness and position of the barrier to achieve high population of the second (antibonding) subband. The particular structure design was based on zero-field numerical self-consistent simulations that predict minimum bonding-antibonding gap for barrier positioned near the node of the first excited state wavefunction (peak of the lowest energy state wavefunction) of the original single-junction. Note that unlike the conventional bilayers realized in double quantum wells or wide single wells our system is intrinsically, strongly anisotropic. At zero magnetic field the lower (bonding) subband wavefunction has dominant weight in the rectangular well while electrons from the higher (antibonding) subband are more likely to occupy the triangular quantum well. Parameters of the two studied samples are summarized in Table I. The partial occupations of the bonding and antibonding subbands at  $B_{\parallel} = 0$  were obtained by Fourier analysis of the low-field SdH oscillations. The Hall measurement at low perpendicular magnetic fields provided an independent check for the total carrier density and was used to determine sample mobilities. The insets in Fig. 1 show the confining potential profiles and wavefunctions of the occupied subbands for two samples.

Sample	$w$ (Å)	$\mu$ ( $10^5$ cm <sup>2</sup> /Vs)	$N_b$	$N_a$ ( $10^{11}$ cm <sup>-2</sup> )	$N_{Hall}$	$\bar{N}$
A	80	2.00	2.46	0.89	3.38	3.4
B	90	2.34	2.77	0.76	3.42	3.5

TABLE I. Sample parameters:  $w$  is the thickness of the rectangular well,  $N_b$  and  $N_a$  are the bonding and antibonding subband densities obtained from SdH measurement,  $N_{Hall}$  is the total 2D electron density derived from low-field Hall data, and  $\bar{N}$  is the average between the SdH and Hall values for the total density used in the numerical simulations.

Magnetotransport data were collected at the temperature 0.45 K and in magnetic fields ranging from 0 to 23 T, using both dc and low-frequency (13 Hz) ac techniques. First, we measured the resistance  $R_{xx}$  for a magnetic field precisely parallel with the 2D layer plane. The recorded magnetoresistance,  $\Delta R_{xx}/R_{xx} = (R_{xx}(B_{\parallel}) - R_{xx}(0))/R_{xx}(0)$ , is plotted in Fig. 1. Consistent with the bilayer nature of the studied samples we observe an oscillation on the magnetoresistance trace with the lower

critical field  $B_{c,1}$  and the upper critical field  $B_{c,2}$ . The values of critical fields are  $B_{c,1} = 5.8$  T,  $B_{c,2} = 11.7$  T for sample A and  $B_{c,1} = 5.9$  T,  $B_{c,2} = 10.7$  T for sample B, respectively. The in-plane magnetic field dependence of subband occupations,  $N_a(B_{\parallel})$  and  $N_b(B_{\parallel})$ , were obtained from SdH oscillation data measured at different field-tilt angles. Typical SdH traces are shown in Fig. 2. In general, the oscillations are not periodic in  $1/B_{\perp}$  ( $B_{\perp}$  is the perpendicular component of the magnetic field) since both  $B_{\perp}$  and  $B_{\parallel}$  vary when the field is swept at a fixed tilt angle. Therefore, the standard Fourier technique does

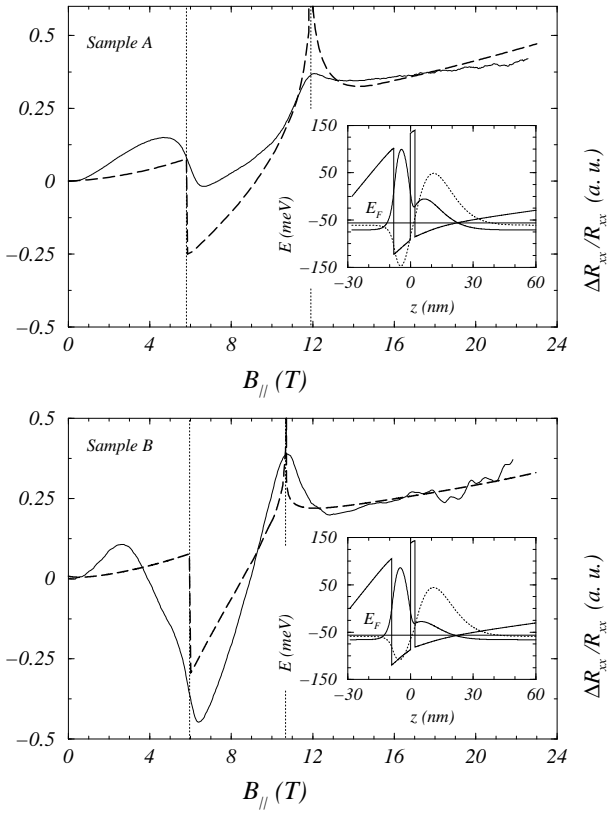


FIG. 1. The magnetoresistance trace (solid line) recorded for samples A and B at in-plane magnetic fields. For both samples the magnetoresistance curve is multiplied by a constant to fit the calculated density of states (dashed line) at high  $B_{\parallel}$ . The insets show the band-profile and the wavefunctions of the bonding and antibonding subbands at  $B = 0$ . The wavefunctions are shifted in the vertical direction so that their asymptotic values match the corresponding quantum levels on the energy axis. In both samples, the levels lie below the Fermi energy,  $E_F$ , indicating two occupied subbands at zero field.

not apply. Instead, we use the measured distance between valleys surrounding individual peaks to identify subband densities.<sup>14</sup> For  $B_{\parallel} < B_{c,1}$  one type of oscillations, corresponding to the lower density (antibonding) subband, can be detected at small tilt angles while two subbands are clearly visible at higher angles. With in-

creasing  $B_{\parallel}$  the distribution of electrons between the two subbands changes, as shown in Fig. 3. Eventually, the antibonding subband is depopulated at  $B_{\parallel} = B_{c,1}$ . At higher in-plane fields two regimes can be distinguished. For  $B_{c,1} < B_{\parallel} < B_{c,2}$  the SdH oscillations are periodic indicating a single occupied subband. Consistently, the corresponding density is equal to the total 2D density measured at zero in-plane magnetic field. The character of the oscillations changes abruptly at  $B_{\parallel} = B_{c,2}$ ; the low in-plane field non-periodicity is recovered and the obtained carrier density is significantly reduced (see Fig. 3). These results suggest that the Fermi sea splits into two disconnected parts of densities that vary with  $B_{\parallel}$ . Only one Fermi surface, however, can be detected from our SdH data.

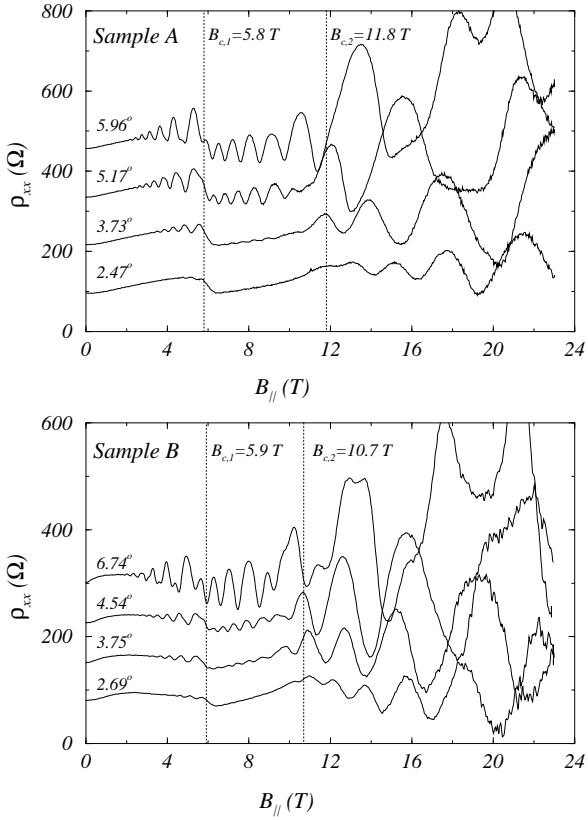


FIG. 2. Typical magnetoresistance traces measured for small angles between the sample plane and the magnetic field direction. The curves for higher angles are shifted upward by 75  $\Omega$ .

### III. THEORETICAL ANALYSIS

The single-particle Hamiltonian for an electron confined in a GaAs/Al<sub>0.3</sub>Ga<sub>0.7</sub>As heterostructure and subjected to in-plane magnetic field can be written as

$$H = \frac{1}{2m^*}(\mathbf{p} + |e|\mathbf{A})^2 + V_{conf}(z), \quad (1)$$

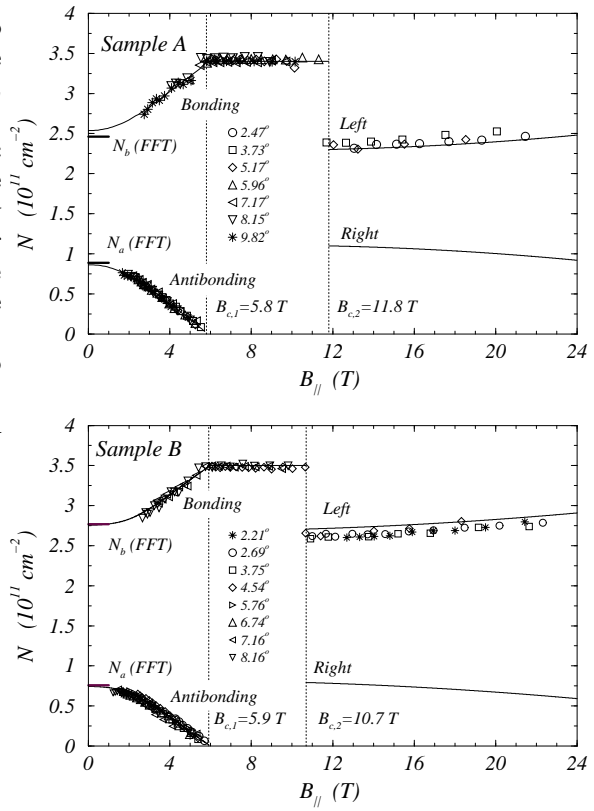


FIG. 3. The 2D electronic concentrations in occupied subbands. Solid lines represent theoretical results, marked points denote data derived from magnetoresistance measurements. Due to strongly field-dependent cyclotron effective masses, measurements at different groups of angles were appropriate for different subbands and different in-plane field regions.  $N_a$  and  $N_b$  denote experimental results obtained from the Fourier transformation of Shubnikov-de Hass oscillations measured at low perpendicular magnetic fields ( $B < 1$ ).

where  $m^*$  is the effective mass in the GaAs conduction band and the vector potential for  $B_{\parallel}$  applied along the  $\hat{y}$ -direction takes a form  $\mathbf{A} = (B_{\parallel}z, 0, 0)$ . The confining potential  $V_{conf}(z)$  is constructed using the nominal growth parameters and includes Hartree and exchange-correlation potentials generated by the free carriers in the quantum wells. The Hartree potential is derived from the  $z$ -dependent density of electrons,  $\rho(z)$ , by numerical solution of the Poisson equation. The exchange-correlation term is calculated within the local-density approximation.<sup>15</sup> In each loop of the self-consistent procedure we solve numerically the Schrödinger equation with the Hamiltonian (1) to get  $\rho(z)$ . Then, a new  $V_{conf}(z)$  is constructed, which enters the next loop of the procedure until the self-consistency condition has been achieved. The resulting energy spectra have the form

$$E_i(\mathbf{k}) = E_{i,x}(k_x) + \frac{\hbar^2}{2m} k_y^2, \quad (2)$$

where  $E_{i,x}(k_x)$  depends on the sample geometry and on the magnitude of the in-plane magnetic field. An index  $i = a, b$  distinguishes the antibonding and bonding subband states.

2D subband concentrations  $N_i$  are proportional to the area enclosed by corresponding Fermi contours. The partial densities of states (DOS)  $g_i$  and the cyclotron effective masses  $m_{c,i}$  are related to the shape of the Fermi contours by the following expression:

$$g_i = \frac{m_{c,i}}{\pi\hbar^2} = \frac{1}{2\pi^2} \oint \frac{dk}{|\nabla_k E_i|}. \quad (3)$$

The total density of states  $g = g_a + g_b$ . The distortion of Fermi lines can be probed experimentally by adding a weak perpendicular component of the magnetic field. For  $B_\perp \ll B_\parallel$ , the quantization of the in-plane component of the electron motion can be described in terms of quasi-classical Landau levels with the cyclotron effective mass given by Eq. (3). The degeneracy of the spin-unresolved levels is  $2|e|B_\perp/\hbar$ .

The evolution of Fermi surfaces in  $B_\parallel$  is illustrated in Fig. 4 for sample B. Fig. 4(a) presents theoretical Fermi contours calculated for several selected values of  $B_\parallel$ , corresponding cyclotron effective masses are shown in Fig. 4(b). The deviations from the zero-field circles reflect the field-induced changes of  $E_{i,x}(k_x)$  described for the case of the simple tight-binding model in Section I. The antibonding  $E_{a,x}(k_x)$  is an asymmetric function of  $k_x$ , narrower than the free-electron parabola, with the minimum (bottom) moving to the Fermi energy which crosses at  $B_\parallel = B_{c,1}$ . The corresponding Fermi contour acquires the shape of a “lens”, i.e. the oval with the longer axis oriented in the  $\hat{k}_y$ -direction. Due to this type of deformation the antibonding cyclotron effective mass  $m_{c,a}$  is a decreasing function of  $B_\parallel$ .

The field-induced local maximum developing in the  $k_x$ -dependence of  $E_{b,x}(k_x)$  causes elongation of the bonding Fermi contour in the  $\hat{k}_x$ -direction. For higher fields, the Fermi line evolves into an asymmetric “peanut” shape. A neck connecting left and right parts of the “peanut” breaks as the saddle point reaches the Fermi energy at  $B_\parallel = B_{c,2}$ . For  $B_\parallel < B_{c,2}$  the bonding effective mass  $m_{c,b}$  grows with  $B_\parallel$  and diverges at the saddle point. Above  $B_{c,2}$ , the Fermi contour splits into two approximately elliptic lines. Very similar results are obtained for sample B.

The position of an electron described by the state  $|i, k_x, k_y\rangle$  in one or the other well is given by  $\langle z \rangle_{i,x} = \langle i, k_x, k_y | z | i, k_x, k_y \rangle$ . The coordinate  $\langle z \rangle_{i,x}$  is related to the  $k_x$ -component of the wave vector by

$$\langle z \rangle_{i,x} = \frac{\hbar k_x}{m\omega} - \frac{\langle v \rangle_{i,x}}{\omega}, \quad (4)$$

$$\langle v \rangle_{i,x} = \frac{1}{\hbar} \frac{\partial E_{i,x}(k_x)}{\partial k_x}, \quad (5)$$

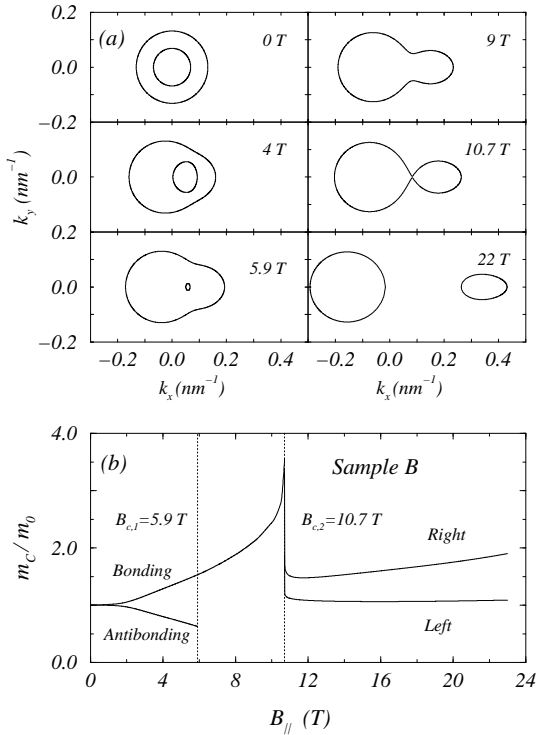


FIG. 4. (a) Theoretical evolution of Fermi contours in the in-plane magnetic field. (b) Self-consistently calculated cyclotron effective masses.

where  $\omega = |e|B_\parallel/m^*$  and  $\langle v \rangle_{i,x}$  is the  $x$ -component of the in-plane group velocity. These relations imply that the larger, almost circular Fermi contour describes the electron layer in the left rectangular well while the smaller elongated oval corresponds to states in the right triangular well. The cyclotron effective masses in two wells are different: above  $B_{c,2}$  the mass for the left well drops quickly close to the zero-field value  $m^*$ , the mass for the triangular well also drops, but to substantially larger value.

Both the partial densities of electrons  $\rho_a(z)$ ,  $\rho_b(z)$  and their sum  $\rho(z) = \rho_a(z) + \rho_b(z)$  are influenced by in-plane magnetic fields. In our structure with a hard-wall barrier the densities have sharp minima in the barrier and peaks inside the wells. The position of peaks is almost the same for all densities and practically field-independent, the magnetic field effect is represented by changes of relative magnitudes of the peaks. We will characterize the transfer of electrons between wells by  $\bar{z}_i(B_\parallel)$ , the field-dependent centroids of electron densities. Results calculated for sample B are shown in Fig. 5. The center of mass of  $\rho(z)$  is in the middle of the structure at  $B_\parallel = 0$  and moves closer to the interface as the field increases. This behavior is typical for single-junction structures.<sup>16</sup> Below  $B_{c,1}$ , the centroid  $\bar{z}_a$  of antibonding electrons is inside the triangular well for all fields. At zero-field,  $\bar{z}_a$  is far from the barrier. The growing  $B_\parallel$  transfers antibonding elec-

trons from the triangular to rectangular well and, consequently,  $\bar{z}_a$  is shifted towards the barrier. The electrons from the bonding subband exhibit opposite behavior in this range of fields: the magnetic field empties the antibonding subband and corresponding electrons, mostly from the triangular well, become a part of the bonding subband. As result,  $\bar{z}_b$  moves from position close to the interface to the position near the barrier as  $B_{\parallel}$  increases. Above  $B_{c,1}$ , when only the bonding subband is occupied, the transfer of electrons from the triangular to rectangular well continues. This is the case also above  $B_{c,2}$  when the bonding Fermi contour is splitted into the left and right parts, as seen in Figs. 3 and 4.

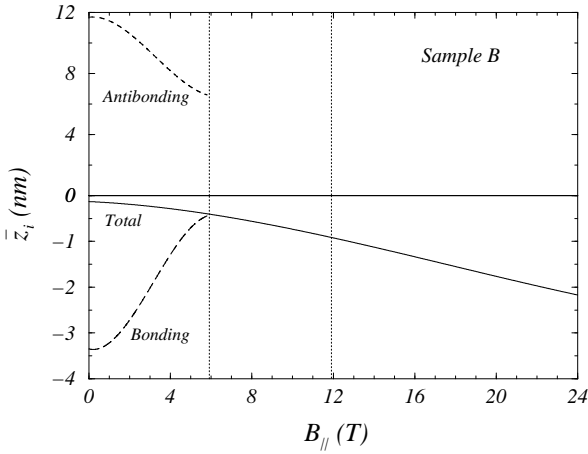


FIG. 5. Theoretical centroids  $\bar{z}_i$ ,  $i = a, b$ , of densities  $\rho_a(z)$ ,  $\rho_b(z)$  and their sum  $\rho(z) = \rho_a(z) + \rho_b(z)$  as functions of in-plane magnetic field. Note the different scales for the positive and negative parts of the vertical axes.

The characteristic of the samples A and B derived from the magnetoresistance experiments are collected in Figs. 1 and 3, together with results of the self-consistent numerical simulation. In the case when theory cannot be directly compared with experiments only the theoretical results for sample B are presented.

We associate the sharp minima in the experimental magnetoresistance traces, presented in Fig. 1 with the sudden decrease of the density of states at  $B_{c,1}$  that contributes to reduction of the scattering rate at the Fermi energy. The difference between the field-dependence of cyclotron effective masses  $m_{c,a}$  and  $m_{c,b}$ , calculated for sample B and shown in Fig. 4(b), explains why the SdH oscillations of electrons in the antibonding subband are seen at lower tilt-angles than the oscillations of electrons from the bonding subband.

The increase of theoretical  $m_{c,b}$  at in-plane fields below  $B_{c,2}$  is related to the strong distortion of the Fermi contour, as seen in Fig 4. Only the bonding subband is occupied for  $B_{c,1} < B_{\parallel} < B_{c,2}$  and, therefore, the SdH oscillations are periodic in  $1/B_{\perp}$ . The decrease of their amplitude for  $B_{\parallel}$  approaching  $B_{c,2}$  is an experimental confirmation of calculated sharp increase of  $m_{c,b}$ . The

theoretical value for the critical in-plane field precisely matches with  $B_{c,2}$  obtained from experiment. The peak in the measured in-plane field magnetoresistance at  $B_{c,2}$  can be understood as a consequence of the divergence of the DOS at Fermi energy or, in other words, of a zero group velocity of electrons at the saddle point.

The experimental magnetoresistance oscillation is clearly associated with van Hove singularities in the  $B_{\parallel}$ -dependent DOS. However, apart from these strong features  $R_{xx}$  does not follow  $g$  for in-plane fields less than  $B_{c,2}$  (see Fig. 1). The differences between  $\Delta R_{xx}/R_{xx}$  and  $\Delta g/g$  curves stem from the in-plane field suppression of the coupling between wells, the transfer of electrons from the triangular to rectangular well, and the changes in the nature of electronic scattering.

At  $B_{\parallel} > B_{c,2}$ , the Fermi contour splits into two approximately elliptic lines. The larger, almost circular Fermi contour is for the rectangular well while the smaller elongated oval corresponds to states in the triangular well. Since electrons are localized in one or the other quantum well, the scattering rate becomes nearly independent of  $B_{\parallel}$ , and  $\Delta R_{xx}/R_{xx} \propto \Delta g/g$  applies, as seen from Fig. 1. Large cyclotron effective mass and low concentration of electrons in the triangular well explain while these states are not detectable by the SdH measurement; at most two weak oscillations can occur in available magnetic fields. The calculated density of electrons in the rectangular well is again in excellent quantitative agreement with SdH data.

#### IV. CONCLUSIONS

We have performed an experimental and theoretical study of asymmetric GaAs/Al<sub>0.3</sub>Ga<sub>0.7</sub>As heterostructure consisting of coupled rectangular and triangular quantum wells. The positions of a strong minimum and maximum in the measured in-plane field dependent resistance of the 2D electron system match precisely with calculated van Hove singularities in the DOS. Theoretical predictions for  $B_{\parallel}$ -dependent occupations of electronic subbands and quantum wells are in quantitative agreement with SdH data recorded at magnetic fields slightly tilted from the 2D layer plane. We conclude that the numerical self-consistent-field technique provides a realistic description of orbital effects of the in-plane field on 2D electron systems confined in semiconductor heterostructures with general growth-direction geometry.

To achieve similar level of accuracy for valence-band states with strong spin-orbit coupling represents a formidable challenge for future theoretical work. Particularly intriguing is the derivation of local-spin-density approximation for many-body states with unequal population of different spin-subbands. Recent remarkable studies of the metal-insulator transition in high mobility GaAs hole systems certainly give a strong motivation for pursuing this kind of research.

This work was supported by the Czech-French project Barrande 99011 and by the Grant Agency of the Czech Republic under Contract No. 202/98/0085.

---

- <sup>1</sup> J. P. Eisenstein, T. J. Gramila, L. N. Pfeiffer, and K. W. West, Phys. Rev. B **44**, 6511 (1991).
- <sup>2</sup> J. Hu and A. H. MacDonald, Phys. Rev. B **46**, 12554 (1992).
- <sup>3</sup> J. A. Simmons, S. K. Lyo, N. E. Harff, and J. F. Klem, Phys. Rev. Lett. **73**, 2256 (1994); S. K. Lyo, Phys. Rev. B **50**, 4965 (1994).
- <sup>4</sup> A. Kurobe, I. M. Castleton, E. H. Linfield, M. P. Grimshaw, K. M. Brown, D. A. Ritchie, M. Pepper, and G. A. C. Jones, Phys. Rev. B, **50**, 11492 (1994).
- <sup>5</sup> T. S. Lay, X. Ying, and M. Shayegan, Phys. Rev. B **52**, R5511 (1995).
- <sup>6</sup> T. Jungwirth, T. S. Lay, L. Smrčka, and M. Shayegan, Phys. Rev. B, **56**, 1029 (1997).
- <sup>7</sup> S. Das Sarma and E. H. Hwang, cond-mat/9909452.
- <sup>8</sup> D. Simonian, S. V. Kravchenko, M. P. Sarachik, and V. M. Pudalov, Phys. Rev. Lett. **79**, 2304 (1997); T. Okamoto, K. Hosoya, S. Kawaji, and a. Yagi, Phys. Rev. Lett. **82**, 3875 (1999).
- <sup>9</sup> Jangsoo Yoon, C. C. Li, D. Shahar, D. C. Tsui, and M. Shayegan, Phys. Rev. Lett., in press (2000).
- <sup>10</sup> S. J. Papadakis, E. P. De Poortere, and M. Shayegan, cond-mat/9911239.
- <sup>11</sup> J. M. Heisz and E. Zaremba, Semicond. Sci. Technol. **8**, 575 (1993).
- <sup>12</sup> T. Jungwirth and L. Smrčka, J. Phys.: Condens. Matter **5**, L217 (1993); L. Smrčka, P. Vašek, J. Koláček, T. Jungwirth, and M. Cukr, Phys. Rev. B **51**, 18011 (1995).
- <sup>13</sup> L. Smrčka, P. Vašek, T. Jungwirth, O. N. Makarovskii, M. Cukr, and L. Jansen, Acta Physica Polonica A, **92** (1997).
- <sup>14</sup> G. R. Facer, B. E. Kane, R. G. Clark, L. N. Pfeiffer, K. W. West, Phys. Rev. B, **82**, R10036 (1997).
- <sup>15</sup> S. H. Vosko, L. Wilk, M. Nusair, Can. J. Phys. **58**, 1200 (1980).
- <sup>16</sup> J. Hampton, J. P. Eisenstein, L. N. Pfeiffer, and K. W. West, Solid State Commun. **94**, 559 (1995); T. Jungwirth and L. Smrčka, Phys. Rev. B, **51**, 10 181 (1995).